



Millisecond dynamics of colloidal suspension studied by X-ray photon correlation spectroscopy at the Shanghai Synchrotron Radiation Facility

Chen-Hui Cui^{2,3} · Zi-Mu Zhou^{3,4} · Lin-Feng Wei⁵ · Song-Lin Li^{2,3} · Feng Tian¹ · Xiu-Hong Li¹ · Zhi Guo¹ · Yi-Hui Xu⁵ · Huai-Dong Jiang^{2,5} · Ren-Zhong Tai^{1,2}

Received: 28 May 2023 / Revised: 5 November 2023 / Accepted: 8 November 2023 / Published online: 21 December 2023
© The Author(s), under exclusive licence to China Science Publishing & Media Ltd. (Science Press), Shanghai Institute of Applied Physics, the Chinese Academy of Sciences, Chinese Nuclear Society 2023

Abstract

X-ray photon correlation spectroscopy (XPCS) has emerged as a powerful tool for probing the nanoscale dynamics of soft condensed matter and strongly correlated materials owing to its high spatial resolution and penetration capabilities. This technique requires high brilliance and beam coherence, which are not directly available at modern synchrotron beamlines in China. To facilitate future XPCS experiments, we modified the optical setup of the newly commissioned BL10U1 USAXS beamline at the Shanghai Synchrotron Radiation Facility (SSRF). Subsequently, we performed XPCS measurements on silica suspensions in glycerol, which were opaque owing to their high concentrations. Images were collected using a high frame rate area detector. A comprehensive analysis was performed, yielding correlation functions and several key dynamic parameters. All the results were consistent with the theory of Brownian motion and demonstrated the feasibility of XPCS at SSRF. Finally, by carefully optimizing the setup and analyzing the algorithms, we achieved a time resolution of 2 ms, which enabled the characterization of millisecond dynamics in opaque systems.

Keywords XPCS · SSRF · Silica suspension · Glycerol · Brownian motion · Millisecond dynamics

This work was supported by National Natural Science Foundation of China (No. 12075304), Natural Science Foundation of Shanghai (No. 22ZR1442100) and National Key Research and Development Program of China (No. 2022YFB3503904).

✉ Zhi Guo
guoz@sari.ac.cn

✉ Yi-Hui Xu
xuyh1@shanghaitech.edu.cn

✉ Ren-Zhong Tai
tairz@sari.ac.cn

¹ Shanghai Synchrotron Radiation Facility, Shanghai Advanced Research Institute, Chinese Academy of Sciences, Shanghai 201204, China

² School of Physical Science and Technology, ShanghaiTech University, Shanghai 201210, China

³ Shanghai Institute of Applied Physics, Chinese Academy of Sciences, Shanghai 201800, China

⁴ University of Chinese Academy of Sciences, Chinese Academy of Sciences, Beijing 100049, China

⁵ Center for Transformative Science, ShanghaiTech University, Shanghai 201210, China

1 Introduction

When coherent light impinges on a disordered sample, the resulting scattered signal forms a speckle pattern. Because the internal structure of the disordered sample evolves over time, the corresponding speckle pattern also fluctuates. Valuable insights into the internal dynamics of the sample can be obtained by analyzing the correlations between these fluctuating speckle patterns. Using this principle, dynamic light scattering (DLS) techniques that utilize coherent visible light have been developed for approximately half a century, facilitating the exploration of numerous intricate dynamics and relaxation processes in condensed systems [1–5]. A fundamental assumption during the correlation of the operational scattering signals is that the photons detected by the detector are scattered only once by the sample, thereby excluding the effect of multiple scattering events. However, in the visible light spectrum, the probability of a single photon undergoing multiple scatterings becomes significant when the concentration of the sample under investigation is excessively high or the sample is optically opaque [6]. Therefore, DLS

is typically utilized only for analyzing materials with low concentrations or minimal absorption.

Owing to this limitation, XPCS techniques that use (partially) coherent X-rays as a substitute for visible light have emerged, thereby enabling the examination of highly concentrated or optically opaque materials [7]. This is primarily because the scattering cross section of X-rays is smaller than that of visible light [8]. This results in reduced susceptibility to multiple scattering during the experiment. In addition, the shorter wavelength of X-rays enables the detection of samples with smaller length scales [9]. However, the smaller scattering cross section of the X-rays also results in a weaker scattering signal. When the number of coherent photons in the (partially) coherent X-ray beam is equivalent to that in a laser, XPCS experiments become more challenging than DLS experiments, resulting in poor signal-to-noise ratio (SNR) of the data obtained. Consequently, the coherent X-ray flux is a primary limiting factor for the development of XPCS. The solution can be derived from the SNR equation [10]:

$$\text{SNR} \propto I_{\text{pix}} \times (N_{\text{pix}} N_{\text{fr}} N_{\text{rep}})^{1/2}. \quad (1)$$

where I_{pix} denotes the average intensity per pixel, which is associated with the incident coherent flux. N_{pix} , N_{fr} , and N_{rep} denote the number of pixels, number of frames, and number of repetitions, respectively. I_{pix} can be enhanced by designing a dedicated XPCS beamline (for instance, focusing the beam using compound refractive lenses). Likewise, the coherent X-ray flux is anticipated to increase by several orders of magnitude by adopting more advanced fourth-generation X-ray sources, such as near diffraction-limited storage rings (DLSRs) [11–16] and free-electron lasers (FELs) [17–22]. N_{pix} can be improved using area detectors along with the multi-speckle XPCS method [23]. Both N_{rep} and N_{fr} enhance the SNR by increasing the number of sampled frames.

Another limitation of the XPCS is its relatively low temporal resolution that primarily arises from the lower (partially) coherent flux employed in XPCS experiments. For instance, at a constant coherent flux, increasing the detector frame rate requires a corresponding reduction in the exposure time, which in turn lowers the value of I_{pix} . According to Eq. 1, this decrease in I_{pix} reduces the SNR. Therefore, both high SNR and high temporal resolution are impossible to achieve simultaneously, as these two factors are inversely related to one another. The temporal resolution of XPCS was constrained to ensure that XPCS experimental data had a sufficiently high SNR. Furthermore, the maximum detection frame rate of the area detectors employed in XPCS experiments presented a notable constraint [7, 9]. With the development of fourth-generation X-ray sources and the introduction of higher-frame-rate detectors, the range of XPCS detection times is expected to expand, particularly for the

fastest dynamics [9, 24, 25]. After more than two decades of development, XPCS has been extensively applied to condensed systems [7, 9], including colloidal suspensions [23, 26], polymers [27, 28], metallic glasses [29, 30], proteins [31–33], and strongly correlated materials [10, 34, 35].

SSRF is the first third-generation synchrotron radiation light source in China. In recent years, its experimental capability has increased [36–40]. More recently, the SSRF commissioned all its second-phase beamlines that employ state-of-the-art undulators to provide significantly higher beam quality. This endeavor will facilitate the development of coherent technology that has already achieved results in coherent diffraction imaging (CDI) and scanning coherent diffraction imaging (scanning CDI or ptychography) at the SSRF [41–43]. However, significant progress is yet to be achieved in XPCS experiments. In addition, the absence of a dedicated XPCS beamline at SSRF presents challenges for conducting XPCS experiments.

In this work, we demonstrated the feasibility of XPCS at the SSRF with millisecond time resolution by optimizing the optics, samples, and analysis algorithm. The experiments employed standard silica colloidal suspensions as samples, which were ideal for XPCS experiments owing to their relatively simple and clear dynamic mechanisms. Furthermore, colloidal particles can serve as tracer particles to reveal structural changes in the sample through their dynamic alterations, such as glass transition [44, 45] and non-equilibrium dynamics of soft materials [46]. Consequently, understanding the dynamic processes of dilute colloidal suspensions is beneficial for further investigations of related materials.

2 Sample preparation

An aqueous suspension of silica spheres (M814153, MACK-LIN, 500 nm) was used as the stock solution in this experiment. Characterized by scanning electron microscopy (SEM), the diameter of the silica spheres of the stock solution was determined by evaluating at least 1000 particles in the image. An average size of $R_{\text{SEM}} = 524.4$ nm and dispersion of $p = 7.2\%$ were obtained [26]. The volume fraction of silica in the stock solution was 1%. But the diffusion of silica in water was too rapid for the Eiger X 4 M detector in the range of the observable. To better characterize the dynamics, the stock solution was mixed with glycerol at a volume ratio of 1:1. Most of the water was removed using a rotary evaporator, yielding considerably slower diffusion [44, 47]. The actual volume fraction of silica was slightly lower than 1% because the rotary evaporator could not completely remove the residual water. The interactions between silica particles can be neglected at this volume fraction [45]. Before the XPCS experiment, the suspension was sonicated and injected into a 2 mm-thick sample cell, which was sealed

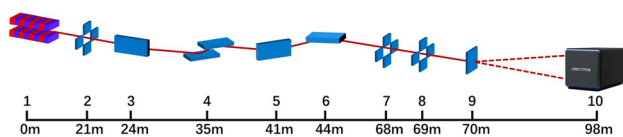


Fig. 1 (Color online) Schematic of the experimental setup: 1. Undulator; 2. Four-blade slits 1; 3. Horizontal deflection mirror; 4. Double multilayer monochromator; 5. Horizontal focusing mirror; 6. Vertical focusing mirror; 7. Four-blade slits 2; 8. Four-blade slits 3; 9. Sample; 10. Detector. [48]

with Kapton film. The experiment was conducted at a temperature of approximately $\sim 298\text{K}$.

3 Experimental configuration

The experiment was conducted at the BL10U1 USAXS beamline of SSRF, and the schematic diagram of the experimental setup is shown in Fig. 1. The incident beam emitted from the undulator was monochromated by a double multilayer monochromator after passing through the four-blade slits 1. The photon energy and energy resolution ($\Delta E/E$) were 10keV ($\lambda = 0.124\text{nm}$) and 5.8×10^{-3} , respectively. The beam was subsequently focused using horizontal and vertical focusing mirrors with the focal point at the detector. The partially coherent light required for the experiment was selected using upstream four-blade slits 2 and 3. A pinhole with a diameter of $100\mu\text{m}$ was placed upstream of the sample to reduce the beam size and increase the coherence of the incident beam on the sample. The scattering signal of the sample was recorded using an area detector (EIGER X 4 M) located 27.6m downstream from the sample. The effective pixel number of the detector was 2070×2167 with a pixel size of $75\mu\text{m} \times 75\mu\text{m}$. Its frame rate could reach 750Hz , i.e., 1.34ms minimum exposure period. In this experiment, the available q -range (scattering wave vector range) was approximately $1.2 \times 10^{-2}\text{nm}^{-1}$ – $2.0 \times 10^{-1}\text{nm}^{-1}$. The scattering wave vector q was determined from the scattering angle 2θ using the formula $q = 4\pi \sin(\theta)/\lambda$. To ensure the repeatability of the experiment and accuracy of the results, the experiments were repeated three times under the same conditions, with each run collecting 1000 speckle patterns. Six exposure periods (2, 5, 10, 20, 50, and 100 ms) were used to evaluate the temporal resolving ability of the XPCS study.

4 DLS

Prior to the XPCS experiment, the silica suspension was pre-characterized using DLS technology. The coherent light source was a laser with a wavelength of $\lambda_{\text{laser}} = 633\text{nm}$, and

the size of the laser beam was adjusted to 2mm using a diaphragm. The laser was then directed into the sample contained in the cuvette, causing the light to scatter and form a speckle pattern. The scattered signal was collected by a detector (photomultiplier tube, PMT) after passing through an order-sorting aperture (OSA) with a diameter of $70\mu\text{m}$. The PMT was located at a scattering angle of $\pi/2$ (90°). The signal was displayed on a computer after correlation using a correlator (ALV-7004/USB-FAST). The entire experimental setup was placed in a dark room to avoid the influence of natural light. Additionally, considering the high sensitivity of the PMT to light, an extra layer of darkroom was added around the detector to prevent stray signals from the laser and allow only the OSA to receive light. The acquisition time for each signal was set to 10s , and the process was repeated ten times to obtain the average value.

The stock solution was diluted with water to different concentrations, and then, these samples were placed in the cuvette for DLS measurement (Fig. 2). The experimental temperature was maintained at 297K . The measured results were fitted (Fig. 2, solid line) using the equation $g^2 - 1 = \beta e^{-2t/\tau}$ to obtain the relaxation time τ , where β represents the speckle contrast. According to the experimental parameters, the hydrodynamic diameters of silica (Fig. 3) can be obtained from the relaxation times τ of the samples. Figure 3 shows that in the case of a low dilution factor, the hydrodynamic diameter of silica first increases and then decreases owing to the influence of multiple scattering. The influence of multiple scattering becomes negligible with increasing dilution factor. The hydrodynamic diameter of silica is stable at approximately 550nm , which is slightly

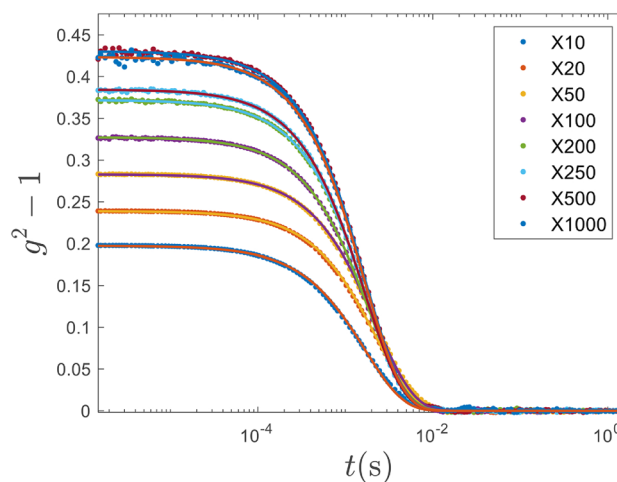


Fig. 2 (Color online) Correlation data (points) obtained using DLS measurements of the stock solution at different dilution factors or concentrations (X10 $\sim 0.1\%$, X20 $\sim 0.05\%$, X50 $\sim 0.02\%$, X100 $\sim 0.01\%$, X200 $\sim 0.005\%$, X250 $\sim 0.004\%$, X500 $\sim 0.002\%$, X1000 $\sim 0.001\%$). These solid lines are the fitting curves for the correlation data

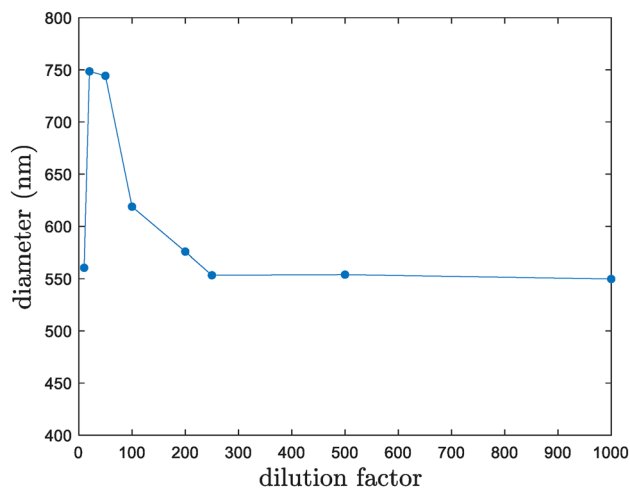


Fig. 3 Hydrodynamic diameters of silica in water suspensions of different concentrations obtained using the fitting results. The x -axis represents the dilution factor of the stock solution

larger than that obtained by SEM. This is consistent with the expected results [23].

These findings indicate that DLS is indeed constrained by the sample concentration and that multiple scattering significantly affects the experimental results. Therefore, determining the dynamic behavior of silica in the stock solution using the traditional DLS method is impossible because of the influence of multiple scattering. However, XPCS can easily overcome the influence of multiple scattering using hard X-rays.

5 Small angle X-ray scattering (SAXS)

The two-dimensional (2D) small angle X-ray scattering (SAXS) data presented in Fig. 4 were generated by overlaying 1000 frames of speckle patterns collected for each of the three sets of data. The results from the three sets of data were averaged. The exposure period was 50 ms, corresponding to a total exposure time of 50 s per frame. The 2D SAXS pattern was azimuthally integrated to obtain the one-dimensional (1D) SAXS profile (Fig. 5 point), illustrating the scattering intensity $I(q)$ with respect to the scattering wave vector q . The signals of bad pixels, gaps, and beamstop were excluded from data processing. By fitting the 1D SAXS data (Fig. 5 line), the diameter of the silica particles was determined to be $R_{\text{SAXS}} = 528.2$ nm (In the high q range, the difference between the SAXS results and fitted curve is primarily because of the weak scattered signal at high q , which is considerably affected by noise.). This size was consistent with that obtained by SEM, indicating that the size of the silica particles produced via rotary evaporation did not change significantly, and substantial agglomeration

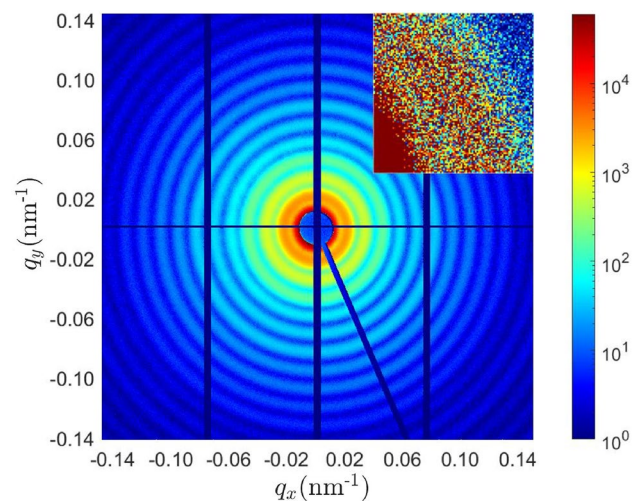


Fig. 4 (Color online) Two-dimensional (2D) SAXS from the sample overlaying 1000 frames collected continuously within 50 s. The result was further averaged from three repeated measurements to improve the statistics. The x - and y -axes are represented by the scattering vectors q_x and q_y , respectively. For a clear view, the logarithm of the scattering signal intensity is taken to the base 10. The illustration in the upper right corner is a speckle image

was not observed. The agreement between the SAXS, SEM, and DLS measurements proves the reliability of the size and structure of the silica particles in the stock solutions. Therefore, a comprehensive understanding of the particle size and potential aggregation phenomena was obtained by employing the SAXS and DLS techniques.

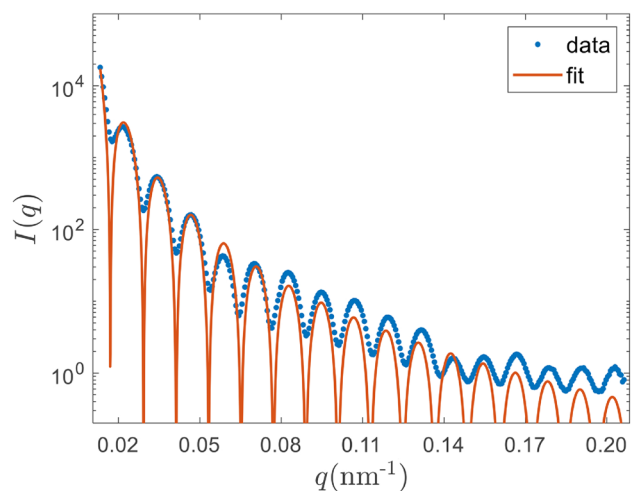


Fig. 5 (Color online) One-dimensional (1D) SAXS data derived by using the azimuthal averaging of scattering signals from the sample shown in Fig. 4. Point: SAXS scattering intensity $I(q)$ with respect to scattering wave vector q ; Line: fitting of silica size (considering the silica as homogeneous spherical particles) [49]. For a clear view, the logarithm of the scattering signal intensity is taken to the base 10

6 X-ray photon correlation spectroscopy (XPCS)

6.1 Theory

To investigate the dynamic properties of silica, the obtained scattering patterns were correlated using the intensity correlation equation. The influence of photon flux variation on the results was minimized by applying the two-time correlation (TTC) method to analyze the sample dynamics [50]:

$$g^2(q, t_1, t_2) = \frac{\langle I(q, t_1)I(q, t_2) \rangle}{\langle I(q, t_1) \rangle \langle I(q, t_2) \rangle}, \tag{2}$$

where $I(q, t_{1,2})$ is the intensity value at q and $t_{1,2}$; $\langle \dots \rangle$ represents the average of all pixels; and $|t_1 - t_2| = \tau$ indicates the delay time. When the sample is in equilibrium during the observation time, the TTC can be expressed as [25, 51]:

$$g^2(q, \tau) = \langle g^2(q, t_1, t_2) \rangle. \tag{3}$$

Averaging the corresponding data with the same delay time τ improves the SNR of the results. The intensity correlation function $g^2(q, \tau)$ can be related to the first-order correlation function $g^1(q, \tau)$ through the Siegert relation [1]:

$$g^2(q, \tau) = 1 + \beta |g^1(q, \tau)|^2. \tag{4}$$

Here, β represents the speckle contrast, which depends on the coherence of the incident beam, optical layout of the beamline and pixel size of the detector. In this study, the diluted colloidal suspension was expected to exhibit Brownian motion [26, 51, 52], such that

$$g^1(q, \tau) = e^{-\Gamma(q)\tau}. \tag{5}$$

Combining Eqs. 4 and 5, the correlation equation can be simplified to:

$$g^2(q, \tau) = 1 + \beta e^{-2\Gamma(q)\tau}. \tag{6}$$

$\Gamma(q) = 1/\tau_c(q)$ represents the relaxation rate, which is the reciprocal of the characteristic relaxation time $\tau_c(q)$:

$$\tau_c(q) = \frac{1}{Dq^2}, \tag{7}$$

D represents the Stokes–Einstein diffusion constant, which can be expressed as

$$D = \frac{k_B T}{6\pi\eta R_H}, \tag{8}$$

where k_B , T , η , and R_H represent the Boltzmann constant, thermodynamic temperature, viscosity coefficient of the

solvent, and hydrodynamic radius of the silica particles, respectively.

6.2 Results and discussion

The two time correlation (TTC) maps in Fig. 6 exhibit no significant change (narrowing) at the midridge line on the diagonal in the image during the entire experiment. This indicates that the silica in the sample is in equilibrium dynamics. Therefore, the effects of sample heating and damage by X-rays on the sample were negligible for the XPCS experiments conducted in this work.

The data collected from the same sample at different exposure periods were correlated and fitted using Eq. 6 (Fig. 7). First, all the data were fitted well using a single exponential model. Second, data with shorter exposure periods exhibited lower SNR. From Eq. 1, it is natural to obtain lower SNR when lower exposure periods reduced the intensity I_{pix} with all other parameters kept constant. Nonetheless, the SNR of the lowest exposure period (2 ms) was sufficient for the correlation analysis. The SNR of the low-exposure periods could be significantly increased by increasing N_{fr} or N_{rep} . Third, and most importantly, despite the significantly different exposure periods, all correlation curves exhibited similar decay behaviors. This is further demonstrated by the relaxation rate analysis below.

The relaxation rate Γ of the sample obtained from fitting is shown in Fig. 8, and the relaxation rates obtained at different exposure periods are consistent. The dashed line is the guide line for the eye, and the error bars are the standard

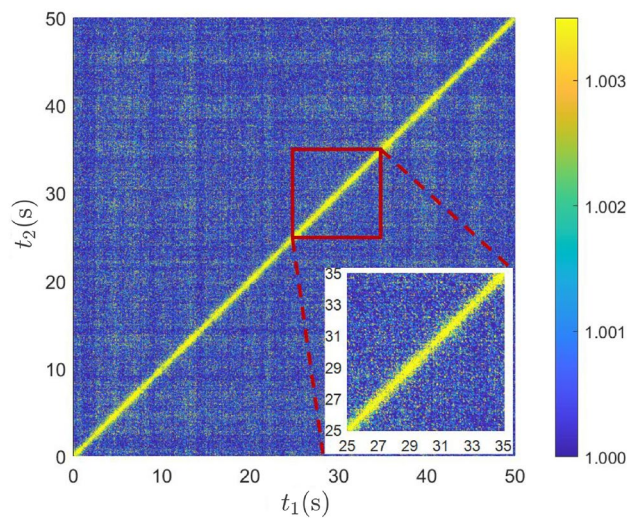


Fig. 6 (Color online) TTC derived from the correlation calculation of 1000 frames of speckle patterns using Eq. 2. $t_{1,2}$ indicates the time of the experiment, where the exposure period is 50 ms, $q = 2.13 \times 10^{-2} \text{ nm}^{-1}$ ($\Delta q = 2.06 \times 10^{-3} \text{ nm}^{-1}$). The inset figure shows a partially enlarged view of the results of the experimental time 25–35 s

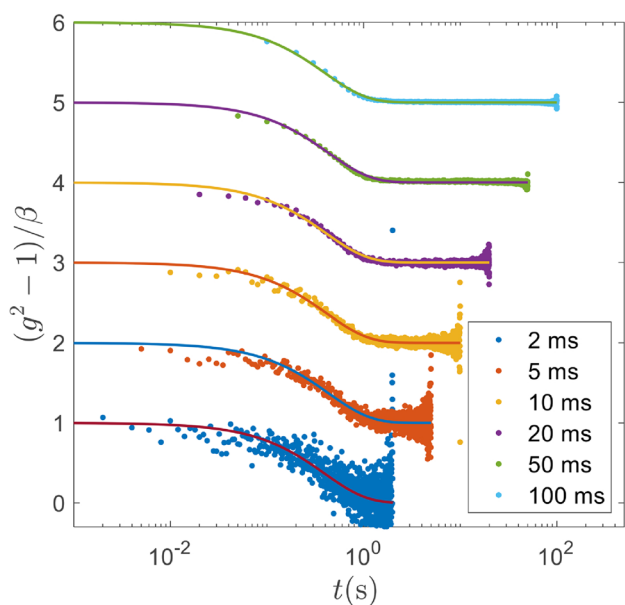


Fig. 7 (Color online) Correlation function of the sample at different exposure periods, where $q = 2.13 \times 10^{-2} \text{ nm}^{-1}$ ($\Delta q = 2.07 \times 10^{-3} \text{ nm}^{-1}$), and $g^2(q, \tau)$ is normalized. For clarity, $g^2(q, \tau)$ was shifted vertically. Points and lines refer to correlation data and fitted curves using Eq. 6, respectively. These results were averaged over three replicated measurements to improve the statistics

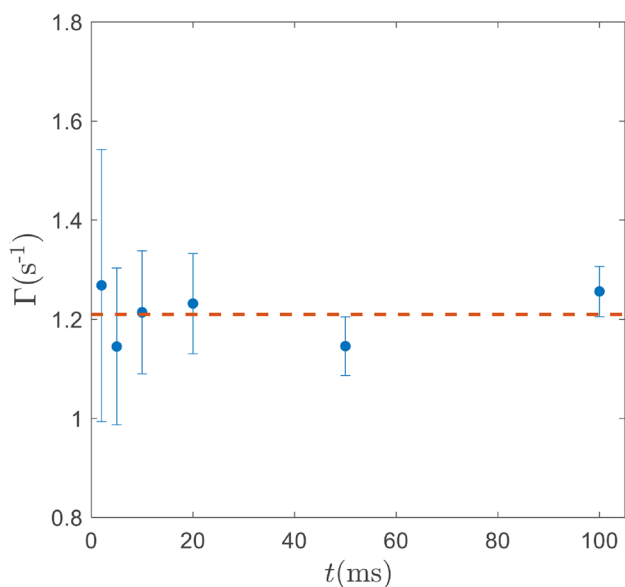


Fig. 8 Relaxation rate Γ obtained by fitting the correlation function at different exposure periods (Fig. 7), and the abscissa represents the different exposure periods (2, 5, 10, 20, 50, and 100 ms). The dashed line is the guide line for the eye. These results were averaged over three replicated measurements to improve the statistics

deviations of the three repetitions. The Γ values for different exposure periods are almost unchanged, indicating the feasibility of XPCS experiments with millisecond exposures in

SSRF [47, 53–56]. In addition, Fig. 8 shows that the standard deviation decreases with increasing exposure time. From Eq. 1, this can be attributed to an increase in I_{pix} , which improves the SNR of the result. Therefore, we can improve the SNR by increasing the number of frames (N_{fr}) collected, thereby reducing the standard deviation of the millisecond exposure results. In summary, the standard deviation of our millisecond-exposure results is usable and can be reduced to ensure realistic dynamic sampling.

The relationship between $g^2(q, \tau)$ and different q values in the data was correlated and fitted using Eq. 6 (Fig. 9). The decay is slower at lower q values because the characteristic decay time decreases with q . Figure 10 shows that the relaxation rate (points) of the sample varies linearly with q^2 . The Stokes–Einstein diffusion constant $D = 2425 \text{ nm}^2/\text{s}$ is obtained by linear fitting with $\Gamma = D \times q^2$. This proves that the silica in the sample undergoes Brownian motion.

Because of the incomplete water removal by the rotary evaporator and the hygroscopicity of glycerol, the sample inevitably contains water. The water content of glycerol strongly affects the viscosity [57], and thus, the viscosity of the sample cannot be accurately determined. However, for a silica sphere, R_{H} is slightly larger than R_{SAXS} [23]. We assumed that $R_{\text{H}} = R_{\text{SAXS}}$ [47] and then estimated the viscosity of the sample using Eq. 8, which yielded $\eta = 0.34 \text{ Pa s}$. Based on the empirical formula [58],

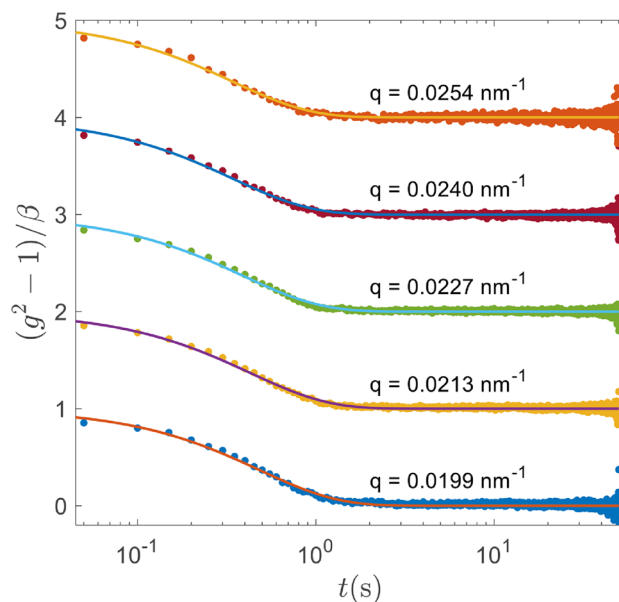


Fig. 9 (Color online) Correlation functions under different scattering wave vector q values ($\Delta q = 6.88 \times 10^{-4} \text{ nm}^{-1}$), where the exposure period is 50 ms, and $g^2(q, \tau)$ is normalized. For clarity, $g^2(q, \tau)$ was shifted vertically. Points and lines refer to correlation data and fitted curves using Eq. 6 at different q values, respectively. These results were averaged over three replicated measurements to improve the statistics

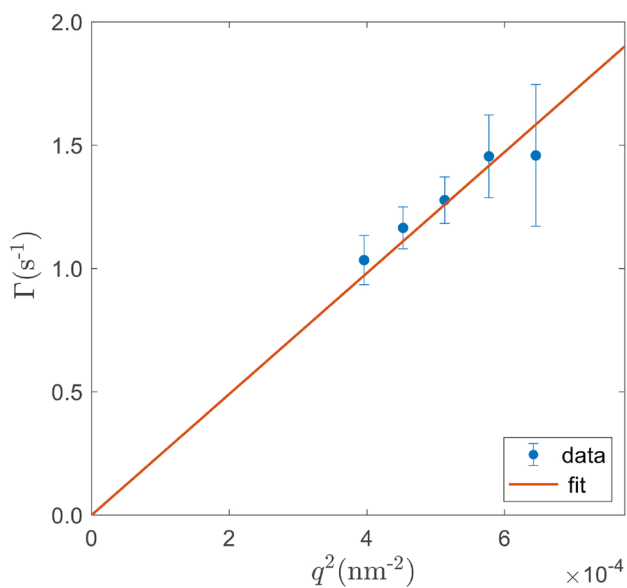


Fig. 10 Relationship between the relaxation rate Γ and q^2 . The points refer to the relaxation rate Γ under different q^2 values obtained from the fitting of Fig. 9. The line refers to the linear fitting of the points, which has been forced through the origin. These results were averaged over three replicated measurements to improve the statistics

$$\eta = \eta_w^\alpha \eta_g^{1-\alpha}, \tag{9}$$

where η_w^α and $\eta_g^{1-\alpha}$ are the viscosities of water and glycerol, respectively, α can be expressed as a function of the glycerol mass concentration C_m :

$$\alpha = 1 - C_m + \frac{abC_m(1 - C_m)}{aC_m + b(1 - C_m)}, \tag{10}$$

a and b are the coefficients of the temperature T_c in Celsius, where $a = 0.705 - 0.0017 T_c$ and $b = (4.9 + 0.036 T_c) a^{2.5}$. The water mass concentration in the sample was estimated to be approximately 5.2%. This portion of water, which is difficult to remove, makes it challenging to determine the viscosity of the sample. Consequently, it is difficult to calculate the hydrodynamic diameter of silica using the Stokes–Einstein diffusion constant D and compare it with the results obtained from SEM or SAXS. Using another solvent that absorbs less water can help solve this problem. Nonetheless, we successfully demonstrated a systematic XPCS study of a highly concentrated silica suspension at SSRF.

7 Summary

XPCS is an emerging technique with great potential for characterizing sample dynamics at molecular and atomic scales. Its advantages over DLS include high penetration

capability, high spatial resolution, and reduced multi-scattering. However, the requirement for coherent X-ray sources limits its accessibility, as third-generation synchrotrons such as SSRF, cannot easily provide sufficient coherence. After the recent upgrade of SSRF, the newly commissioned BL10U1 USAXS beamline provides an ideal platform for XPCS experiments because of its unique properties such as relatively high coherence, high brilliance, and long sample-to-detector distance.

In this study, we successfully performed XPCS studies on a silica suspension model system. The linear $\Gamma - q^2$ dependence demonstrates that the correct Brownian motion dynamics was obtained. Careful collimation of micrometer optics ensured low parasitic scattering and high coherence, and a newly established framework for data analysis enabled the effective extraction of dynamic information from scattering images. Consequently, we achieved a millisecond time resolution, which is at the same level as most XPCS experiments at modern synchrotrons.

The establishment of the XPCS platform is expected to provide new options for researchers in China and abroad and facilitate the study of various nanoscale and micro-scale samples such as colloidal suspensions, polymers, glass, biomacromolecules, and strongly related materials. This powerful tool will enable researchers gain valuable insights into the dynamic properties of these systems in their natural environment and contribute to a deeper understanding of their behavior and properties.

Acknowledgements The authors thank the staff of USAXS beamline (BL10U1) at SSRF for their support during the beamtime. The authors thank the user experimental assistance system of SSRF for their assistance.

Author Contributions Huai-Dong Jiang, and Ren-Zhong Tai contributed to the overall research concept and supervision of this study. Yi-Hui Xu, Chen-Hui Cui, Zi-Mu Zhou, Lin-Feng Wei, and Song-Lin Li participated in material preparation, data collection, data processing program writing, and data analysis. Feng Tian, Xiu-Hong Li provided experimental suggestions and optimized experimental conditions. Zhi Guo and Yi-Hui Xu provided fund support and reviewed the manuscript. The first draft of the manuscript was written by Chen-Hui Cui, and all authors commented on previous versions of the manuscript. All authors read and approved the final manuscript.

Data Availability Statement The data that support the findings of this study are openly available in Science Data Bank at <https://doi.org/10.57760/sciencedb.13559> and <https://cstr.cn/31253.11.sciencedb.13559>.

Declarations

Conflict of interest Ren-Zhong Tai is an editorial board member for Nuclear Science and Techniques and was not involved in the editorial review, or the decision to publish this article. All authors declare that there are no competing interests.

References

- B.J. Berne, R. Pecora, *Dynamic Light Scattering: With Applications to Chemistry, Biology, and Physics* (Wiley, Hoboken, 2000)
- R. Yan, Z. Guo, R.Z. Tai et al., Observation of long range correlation dynamics in BaTiO₃ near TC by photon correlation spectroscopy. *Appl. Phys. Rev.* **93**, 192908 (2008). <https://doi.org/10.1063/1.3025465>
- C.L. Song, R. Yan, Z. Guo et al., Temperature dependence of relaxation time for polarization clusters in BaTiO₃ near TC. *Nucl. Tech.* **33**(4), 258–261 (2010). ((in Chinese))
- R. Yan, Z. Guo, R.Z. Tai, Observation of relaxation time for polarization clusters in BaTiO₃ near TC by photon correlation spectroscopy. *Nucl. Tech.* **32**(6), 439–442 (2009). ((in Chinese))
- M.J. Zhang, Z. Guo, R.Z. Tai et al., Observation of dual relaxation dynamics of polarization clusters in barium titanate by photon correlation spectroscopy. *Jpn. J. Appl. Phys.* **54**(4), 042401 (2015). <https://doi.org/10.7567/JJAP.54.042401>
- P.N. Segrè, O.P. Behrend, P.N. Pusey, Short-time Brownian motion in colloidal suspensions: experiment and simulation. *Phys. Rev. E.* **52**(5), 5070 (1995). <https://doi.org/10.1103/PhysRevE.52.5070>
- G. Grübel, F. Zontone, Correlation spectroscopy with coherent X-rays. *J. Alloys Compd.* **362**(1–2), 3–11 (2004). [https://doi.org/10.1016/S0925-8388\(03\)00555-3](https://doi.org/10.1016/S0925-8388(03)00555-3)
- D. Lumma, L.B. Lurio, S.G.J. Mochrie, Area detector based photon correlation in the regime of short data batches: data reduction for dynamic x-ray scattering. *Rev. Sci. Instrum.* **71**(9), 3274–3289 (2000). <https://doi.org/10.1063/1.1287637>
- O.G. Shpyrko, X-ray photon correlation spectroscopy. *J. Synchrotron. Radiat.* **21**(5), 1057–1064 (2014). <https://doi.org/10.1107/S1600577514018232>
- J.R. Massey, R.C. Temple, T.P. Almeida et al., Asymmetric magnetic relaxation behavior of domains and domain walls observed through the FeRh first-order metamagnetic phase transition. *Phys. Rev. B* **102**(14), 144304 (2020). <https://doi.org/10.1103/PhysRevB.102.144304>
- C.G. Schroer, I. Agapov, W. Brefeld et al., PETRA IV: the ultralow-emittance source project at DESY. *J. Synchrotron. Radiat.* **25**(5), 1277–1290 (2018). <https://doi.org/10.1107/S1600577518008858>
- J.B. Svensson, T.K. Charles, O. Lundh et al., Third-order double-achromat bunch compressors for broadband beams. *Phys. Rev. Accel. Beams* **22**(10), 104401 (2019). <https://doi.org/10.1103/PhysRevAccelBeams.22.104401>
- D. Chenevier, A. Joly, ESRF: inside the extremely brilliant source upgrade. *Synchrotron Radiat. News* **31**(1), 32–35 (2018). <https://doi.org/10.1080/08940886.2018.1409562>
- J. Dooling, M. Borland, W. Berg et al., Collimator irradiation studies in the Argonne Advanced Photon Source at energy densities expected in next-generation storage ring light sources. *Phys. Rev. Accel. Beams* **25**(4), 043001 (2022). <https://doi.org/10.1103/PhysRevAccelBeams.25.043001>
- Y. Jiao, G. Xu, X.H. Cui et al., The HEPS project. *J. Synchrotron Radiat.* **25**(6), 1611–1618 (2018). <https://doi.org/10.1107/S1600577518012110>
- Z.H. Bai, G.W. Liu, T.L. He et al., Preliminary physics design of the Hefei advanced light facility storage ring. *High Power Laser Part. Beams* **34**, 104003 (2022). <https://doi.org/10.11884/HPLPB202234.220137>
- T. Tschentscher, C. Bressler, J. Grünert et al., Photon beam transport and scientific instruments at the European XFEL. *Appl. Sci.* **7**(6), 592 (2017). <https://doi.org/10.3390/app7060592>
- A. Halavanau, F.J. Decker, C. Emma et al., Very high brightness and power LCLS-II hard X-ray pulses. *J. Synchrotron. Radiat.* **26**(3), 635–646 (2019). <https://doi.org/10.1107/S1600577519002492>
- C.J. Milne, T. Schietinger, M. Aiba et al., SwissFEL: the Swiss X-ray free electron laser. *Appl. Sci.* **7**(7), 720 (2017). <https://doi.org/10.3390/app7070720>
- M. Yabashi, H. Tanaka, K. Tono et al., Status of the SACLA facility. *Appl. Sci.* **7**(6), 604 (2017). <https://doi.org/10.3390/app7060604>
- Z.T. Zhao, D. Wang, Q. Gu et al., Status of the SXFEL facility. *Appl. Sci.* **7**(6), 607 (2017). <https://doi.org/10.3390/app7060607>
- Y.X. Zhang, J.F. Chen, D. Wang, RF design optimization for the SHINE 3.9 GHz cavity. *Nucl. Sci. Tech.* **31**(7), 73 (2020). <https://doi.org/10.1007/s41365-020-00772-z>
- J. Möller, Y. Chushkin, S. Prevost et al., Multi-speckle X-ray photon correlation spectroscopy in the ultra-small-angle X-ray scattering range. *J. Synchrotron Radiat.* **23**(4), 929–936 (2016). <https://doi.org/10.1107/S1600577516008092>
- K. Switalski, J. Fan, L. Li et al., Direct measurement of Stokes–Einstein diffusion of Cowpea mosaic virus with 19 μs-resolved XPCS. *J. Synchrotron Radiat.* **29**, 1429–1435 (2022). <https://doi.org/10.1107/S1600577522008402>
- S.K. Sinha, Z. Jiang, L.B. Lurio et al., X-ray photon correlation spectroscopy studies of surfaces and thin films. *Adv. Mater.* **26**(46), 7764–7785 (2014). <https://doi.org/10.1002/adma.201401094>
- S.B. Dierker, R. Pindak, R.M. Fleming et al., X-ray photon correlation spectroscopy study of Brownian motion of gold colloids in glycerol. *Phys. Rev. Lett.* **75**(3), 449 (1995). <https://doi.org/10.1103/PhysRevLett.75.449>
- T. Hoshino, D. Murakami, Y. Tanaka et al., Dynamical crossover between hyperdiffusion and subdiffusion of polymer-grafted nanoparticles in a polymer matrix. *Phys. Rev. E.* **88**(3), 032602 (2013). <https://doi.org/10.1103/PhysRevE.88.032602>
- J. Carnis, W. Cha, J. Wingert et al., Demonstration of feasibility of x-ray free electron laser studies of dynamics of nanoparticles in entangled polymer melts. *Sci. Rep.* **4**(1), 6017 (2014). <https://doi.org/10.1038/srep06017>
- Z. Evenson, B. Ruta, S. Hechler et al., X-ray photon correlation spectroscopy reveals intermittent aging dynamics in a metallic glass. *Phys. Rev. Lett.* **115**(17), 175701 (2015). <https://doi.org/10.1103/PhysRevLett.115.175701>
- B. Ruta, Y. Chushkin, G. Monaco et al., Atomic-scale relaxation dynamics and aging in a metallic glass probed by x-ray photon correlation spectroscopy. *Phys. Rev. Lett.* **109**(16), 165701 (2012). <https://doi.org/10.1103/PhysRevLett.109.165701>
- M. Reiser, A. Girelli, A. Ragulskaya et al., Resolving molecular diffusion and aggregation of antibody proteins with megahertz X-ray free-electron laser pulses. *Nat. Commun.* **13**(1), 5528 (2022). <https://doi.org/10.1038/s41467-022-33154-7>
- L.B. Lurio, G.M. Thurston, Q. Zhang et al., Use of continuous sample translation to reduce radiation damage for XPCS studies of protein diffusion. *J. Synchrotron Radiat.* **28**(2), 490–498 (2021). <https://doi.org/10.1107/S1600577521000035>
- J. Möller, M. Sprung, A. Madsen et al., X-ray photon correlation spectroscopy of protein dynamics at nearly diffraction-limited storage rings. *IUCrJ.* **6**(5), 794–803 (2019). <https://doi.org/10.1107/S2052252519008273>
- R.Z. Tai, K. Namikawa, M. Kishimoto et al., Picosecond snapshot of the speckles from ferroelectric BaTiO₃ by means of X-ray lasers. *Phys. Rev. Lett.* **89**(25), 257602 (2002). <https://doi.org/10.1103/PhysRevLett.89.257602>
- K. Namikawa, M. Kishimoto, K. Nasu et al., Direct observation of the critical relaxation of polarization clusters in BaTiO₃ using a pulsed X-ray laser technique. *Phys. Rev. Lett.* **103**(19), 197401 (2009). <https://doi.org/10.1103/PhysRevLett.103.197401>

36. Z.J. Qiu, K. Li, H.L. Xie et al., Study of 20 Hz high spatial-temporal resolution monochromatic X-ray dynamic micro-CT. *Nucl. Tech.* **46**(7), 070101 (2023). <https://doi.org/10.11889/j.0253-3219.2023.hjs.46.070101>. (in Chinese)
37. H.T. Li, B. Zhao, X.Z. Zhang et al., Development of a portable laser heating device for synchrotron radiation in situ experiment. *Nucl. Tech.* **46**(2), 020101 (2023). <https://doi.org/10.11889/j.0253-3219.2023.hjs.46.020101>. (in Chinese)
38. H.Z. Liu, L. Ji, S.Q. Gu et al., Upgrade of transmission XAFS data acquisition system upgrade of Shanghai Synchrotron Radiation Facility BL14W1 beamline station. *Nucl. Tech.* **45**(7), 070103 (2022). <https://doi.org/10.11889/j.0253-3219.2022.hjs.45.070103>. (in Chinese)
39. S.S. Qu, Z. Guo, R.Z. Tai et al., Design of soft X-ray photon correlation spectroscopy device. *Nucl. Tech.* **42**(4), 040103 (2019). <https://doi.org/10.11889/j.0253-3219.2019.hjs.42.040103>. (in Chinese)
40. X. Yang, J.F. Cao, J.Q. Li et al., Picosecond time-resolved X-ray ferromagnetic resonance measurements at Shanghai Synchrotron Radiation Facility. *Nucl. Sci. Tech.* **33**(5), 63 (2022). <https://doi.org/10.1007/s41365-022-01037-7>
41. Z.J. Xu, C.P. Wang, H.G. Liu et al., Low-dose, high-resolution and high-efficiency ptychography at STXM beamline of SSRF. *J. Phys. Conf. Ser.* **849**(1), 012033 (2017). <https://doi.org/10.1088/1742-6596/849/1/012033>
42. C.P. Wang, Z.J. Xu, H.G. Liu et al., Soft X-ray ptychography method at SSRF. *Nucl. Sci. Tech.* **28**(6), 74 (2017). <https://doi.org/10.1007/s41365-017-0227-6>
43. G.Z. Zhou, Z. Hu, S.M. Yang et al., Preliminary exploration of hard X-ray coherent diffraction imaging method at SSRF. *Acta Phys. Sin.* **69**(3), 034102 (2020). <https://doi.org/10.7498/aps.69.20191586>
44. C. Caronna, Y. Chushkin, A. Madsen et al., Dynamics of nanoparticles in a supercooled liquid. *Phys. Rev. Lett.* **100**(5), 055702 (2008). <https://doi.org/10.1103/PhysRevLett.100.055702>
45. H. Conrad, F. Lehmkuehler, B. Fischer et al., Correlated heterogeneous dynamics in glass-forming polymers. *Phys. Rev. E.* **91**(4), 042309 (2015). <https://doi.org/10.1103/PhysRevE.91.042309>
46. E.B. Trigg, L. Wiegart, A. Fluerasu et al., Dynamics of polymerization and gelation in epoxy nanocomposites via X-ray photon correlation spectroscopy. *Macromolecules* **54**(13), 6575–6584 (2021). <https://doi.org/10.1021/acs.macromol.1c00727>
47. F. Lehmkuehler, P. Kwaśniewski, W. Roseker et al., Sequential single shot x-ray photon correlation spectroscopy at the SACLA free electron laser. *Sci. Rep.* **5**(1), 17193 (2015). <https://doi.org/10.1038/srep17193>
48. Z. Hu, C.X. Hong, W.Q. Hua et al., Online monitoring of hard X-ray beam at SSRF. *Acta Opt. Sin.* **41**(15), 1534001 (2021). <https://doi.org/10.3788/AOS202141.1534001>
49. J. Als-Nielsen, D. McMorrow, *Elements of Modern X-Ray Physics* (Wiley, Hoboken, 2011), pp.113–146
50. M. Sutton, K. Laaziri, F. Livet et al., Using coherence to measure two-time correlation functions. *Opt. Express.* **11**(19), 2268–2277 (2003). <https://doi.org/10.1364/OE.11.002268>
51. F. Lehmkuehler, W. Roseker, G. Grübel, From femtoseconds to hours-measuring dynamics over 18 orders of magnitude with coherent x-rays. *Appl. Sci.* **11**(13), 6179 (2021). <https://doi.org/10.3390/app11136179>
52. Y. Xu, M. Sikorski, J.D. Fan et al., Thermal effects of beam profiles on X-ray photon correlation spectroscopy at megahertz X-ray free-electron lasers. *Opt. Express* **30**(23), 42639–42648 (2022). <https://doi.org/10.1364/OE.464852>
53. W. Jo, R. Rysov, F. Westermeier et al., Demonstration of 3D photon correlation spectroscopy in the hard X-ray regime. *Opt. Lett.* **47**(2), 293–296 (2022). <https://doi.org/10.1364/OL.444190>
54. G.X. Ju, D.W. Xu, M.J. Highland et al., Coherent X-ray spectroscopy reveals the persistence of island arrangements during layer-by-layer growth. *Nat. Phys.* **15**(6), 589–594 (2019). <https://doi.org/10.1038/s41567-019-0448-1>
55. F. Dallari, A. Jain, M. Sikorski et al., Microsecond hydrodynamic interactions in dense colloidal dispersions probed at the European XFEL. *IUCrJ.* **8**(5), 775–783 (2021). <https://doi.org/10.1107/S2052252521006333>
56. M. Reiser, J. Hallmann, J. Moller et al., Photo-controlled dynamics and transport in entangled wormlike micellar nanocomposites studied by XPCS. *Macromolecules* **55**(19), 8757–8765 (2022). <https://doi.org/10.1021/acs.macromol.2c01326>
57. J.B. Segur, H.E. Oberstar, Viscosity of glycerol and its aqueous solutions. *Ind. Eng. Chem.* **43**(9), 2117–2120 (1951). <https://doi.org/10.1021/ie50501a040>
58. N.S. Cheng, Formula for the viscosity of a glycerol–water mixture. *Ind. Eng. Chem. Res.* **47**(9), 3285–3288 (2008). <https://doi.org/10.1021/ie071349z>

Springer Nature or its licensor (e.g. a society or other partner) holds exclusive rights to this article under a publishing agreement with the author(s) or other rightsholder(s); author self-archiving of the accepted manuscript version of this article is solely governed by the terms of such publishing agreement and applicable law.